Smoothened and ARL13B are critical in mouse for

superior cerebellar peduncle targeting

Sarah K. Suciu^{*,†,‡} Alyssa B. Long^{†,‡} and Tamara Caspary[†]

^{*}Genetics and Molecular Biology Graduate Program, [†]Department of Human Genetics,

Emory University, Atlanta, GA 30322, [‡]These authors contributed equally

ORCID ID:

Suciu: 0000-0002-2416-9519 Long: 0000-0002-4467-4213 Caspary: 0000-0002-6579-7589

Summary statement

Joubert syndrome is diagnosed by the hindbrain "molar tooth sign" malformation. Using mouse models, we show loss of the ciliary GTPase ARL13B, mutations in which lead to Joubert syndrome, result in two features of the molar tooth sign: hypoplasia of the cerebellar vermis and inappropriate targeting of the superior cerebellar peduncles. Furthermore, we demonstrate that loss of vertebrate Hedgehog signaling may be the underlying disrupted mechanism as we extend its role in axon guidance to the superior cerebellar peduncles.

Running title (~35 characters, including spaces):

SMO and ARL13B in SCP targeting

Key words/phrases (up to ten):

molar tooth sign, Joubert syndrome, Smo, ARL13B, SCP targeting, cerebellar vermis

Corresponding author:

Tamara Caspary

Department of Human Genetics

615 Michael Street, Suite 301

Atlanta, GA 30322

404-727-9862

tcaspar@emory.edu

1 Abstract

2 Patients with the ciliopathy Joubert syndrome present with physical anomalies, 3 intellectual disability, and a hindbrain malformation described as the "molar tooth sign" 4 due to its appearance on an MRI. This radiological abnormality results from a 5 combination of hypoplasia of the cerebellar vermis and inappropriate targeting of the 6 white matter tracts of the superior cerebellar peduncles. ARL13B is a cilia-enriched 7 regulatory GTPase established to regulate cell fate, cell proliferation and axon guidance 8 through vertebrate Hedgehog signaling. In patients, mutations in ARL13B cause Joubert 9 syndrome. In order to understand the etiology of the molar tooth sign, we used mouse 10 models to investigate the role of ARL13B during cerebellar development. We found 11 ARL13B regulates superior cerebellar peduncle targeting and these fiber tracts require 12 Hedgehog signaling for proper guidance. However, in mouse the Joubert-causing R79Q 13 mutation in ARL13B does not disrupt Hedgehog signaling nor does it impact tract 14 targeting. We found a small cerebellar vermis in mice lacking ARL13B function but no 15 cerebellar vermis hypoplasia in mice expressing the Joubert-causing R79Q mutation. 16 Additionally, mice expressing a cilia-excluded variant of ARL13B that transduces 17 Hedgehog normally, showed normal tract targeting and vermis width. Taken together, 18 our data indicate that ARL13B is critical for control of cerebellar vermis width as well as 19 superior cerebellar peduncle axon guidance, likely via Hedgehog signaling. Thus, our 20 work highlights the complexity of ARL13B in molar tooth sign etiology.

21 INTRODUCTION

22 Joubert Syndrome and Related Disorders (JSRD) are recessive congenital 23 disorders with a variety of symptoms including developmental delay, intellectual 24 disability, abnormal respiratory rhythms, ataxia, oculomotor apraxia, polydactyly, 25 craniofacial defects, retinal dystrophy, nephronophthisis, and hepatic fibrosis (Parisi et 26 al. 2007, Bachmann-Gagescu et al. 2020). While the exact prevalence of JSRD is not 27 known, published statistics range from 1:80,000 to 1:100,000, but these may be 28 underestimates as suggested by a recent study (Brancati et al. 2010, Nuovo et al. 29 2020). The characteristic neuroanatomical feature of JSRD is the molar tooth sign 30 (MTS), which is caused by hypoplasia of the cerebellar vermis and thickened, elongated 31 superior cerebellar peduncles (SCPs) that fail to decussate (Maria et al. 1997;Yachnis 32 and Rorke 1999; Poretti et al. 2007). However, little is known about the mechanistic 33 etiology of this hindbrain malformation. This is especially significant as several 34 symptoms of JSRD arise from defects in the hindbrain: cerebellar dysfunction 35 commonly causes ataxia and hypotonia, while some patients manifest life-threatening 36 breathing problems (Parisi 2019).

To date, mutations in over 35 genes cause JSRD, and their associated proteins almost always localize to the primary cilium or the centrosome (Parisi 2019). Thus, JSRD is classified as a ciliopathy, a category of human disease stemming from ciliary dysfunction. One of the genes implicated in JSRD is *ARL13B*, which encodes a regulatory GTPase highly enriched in cilia (Cantagrel *et al.* 2008; Bachmann-Gagescu *et al.* 2015; Thomas *et al.* 2015; Shaheen *et al.* 2016; Rafiullah *et al.* 2017). As a GTPase, ARL13B is expected to have multiple effector proteins which interact with

specific ARL13B residues. ARL13B can function as a guanine exchange factor (GEF) 44 45 for ARL3, mutations in which also lead to JSRD (Gotthardt et al. 2015; Ivanova et al. 46 2017). JSRD-causing mutations in either ARL3 or ARL13B can disrupt their interaction 47 or ARL13B's GEF activity, consistent with the notion that specific ARL13B function is 48 affected by JS-causing point mutations (Gotthardt et al. 2015; Ivanova et al. 2017; 49 Alkanderi et al. 2018). Most JSRD-causing ARL13B mutations cluster within the 50 protein's GTPase domain, although two are located in the coiled coil domains in the C 51 terminal half of the protein (Cantagrel et al. 2008; Bachmann-Gagescu et al. 2015; 52 Thomas et al. 2015; Shaheen et al. 2016; Rafiullah et al. 2017). ARL13B complexes 53 with the inositol phosphatase INPP5E, which is also implicated in causing JSRD (Bielas et al. 2009; Humbert et al. 2012). ARL13B is critical for targeting INPP5E to cilia and 54 55 JSRD-causing ARL13B mutations disrupt INPP5E ciliary targeting (Humbert et al. 56 2012). INPP5E controls ciliary lipid composition through its phosphatase activity and 57 most JSRD-causing mutations are within its phosphatase domain (Bielas et al. 2009; 58 Chavez et al. 2015; Garcia-Gonzalo et al. 2015). Other proteins implicated in JSRD also 59 affect ciliary targeting with many functioning at the transition zone, supporting the notion 60 that abnormal ciliary traffic leading to defective signaling underlies JSRD (Arts et al. 61 2007; Delous et al. 2007; Garcia-Gonzalo et al. 2011; Hopp et al. 2011; Srour et al. 62 2012; Roberson et al. 2015).

The mechanistic connection between the cilia-related proteins implicated in
 JSRD and the MTS are elusive in part because distinct biological processes are at play.
 Abnormal proliferation may underlie the hypoplastic cerebellar vermis whereas defective
 axonal targeting is likely involved in the abnormal SCP tracts. One signaling pathway

potentially linked to both processes is vertebrate Hedgehog (Hh) which relies on cilia 67 68 (Huangfu et al. 2003). Sonic hedgehog (Shh) is a mitogenic cue that controls 69 proliferation in the developing cerebellum so its misregulation could underlie the 70 cerebellar hypoplasia (Dahmane and Ruiz i Altaba 1999; Wechsler-Reya and Scott 71 1999; Kenney and Rowitch 2000). While the SCP tracts that normally project from the 72 deep cerebellar nuclei to the contralateral thalamus are guided by unknown signals, 73 Shh is a known commissural axon guidance cue (Charron et al. 2003). JSRD patients 74 can also display axon guidance defects in decussation of the pyramidal tracts (Yachnis 75 and Rorke 1999; Poretti et al. 1997). 76 ARL13B and INPP5E, encoding ciliary proteins linked to JSRD, are known to regulate vertebrate Hh signaling. In mouse models, ARL13B loss disrupts cell fate 77 78 specification in the neural tube, proliferation of the cerebellar granule precursor cells in 79 the cerebellum and Shh-directed guidance of commissural axons in the spinal cord 80 (Caspary et al. 2007; Bay et al. 2018; Ferent et al. 2019). These data support a model 81 whereby disruption of Shh signaling by ARL13B mutation could provide a single 82 mechanism underlying the MTS. This model is bolstered by the fact that additional 83 phenotypes exhibited by JSRD patients, such as craniofacial defects or polydactyly, can 84 arise from aberrant Hh signaling (Valente et al. 2008; Lan and Jiang 2009; Lipinski et al. 85 2010). 86 As attractive as a Hh-based model for JSRD may be, not all the data support that

As attractive as a Hn-based model for JSRD may be, not all the data support that
 JSRD phenotypes result from misregulation of Hh signaling. Some features of JSRD,
 such as the renal and liver anomalies, are not clearly due to misregulation of Hh
 signaling (Doherty 2009; Breslow *et al.* 2018). Additionally, of over 35 genes implicated

90 in JSRD, only 22 play some role in Hh pathway regulation (Davey et al. 2006; Reiter 91 and Skarnes 2006; Caspary et al. 2007; Vierkotten et al. 2007; Huang et al. 2009; 92 Weatherbee et al. 2009; Bimonte et al. 2011; Dowdle et al. 2011; Sang et al. 2011; Chih 93 et al. 2011; Christopher et al. 2012; Thomas et al. 2012; Abdelhamed et al. 2013; Hynes 94 et al. 2014; Wu et al. 2014; Chavez et al. 2015; Garcia-Gonzalo et al. 2015; Asadollahi 95 et al. 2018; Frikstad et al. 2019; Munoz-Estrada and Ferland 2019). Some of these links 96 are tenuous. For example, mouse Arl3 mutants mislocalize the Hh transcription factor, 97 GLI3, in their cilia yet do not exhibit any of the phenotypes normally displayed by 98 mutants in the Hh pathway (Schrick et al. 2006, Lai et al. 2011; Schwarz et al. 2017). 99 Additional signaling pathways are linked to cilia including others known to be important 100 in cell proliferation and axon guidance. Loss of either of the JSRD-linked genes Ahi1 or 101 Cep290 in mouse leads to a small cerebellar vermis due to aberrant Wht signaling 102 (Lancaster et al. 2011; Ramsbottom et al. 2020). Possible JSRD-causing mutations in 103 Znf423 are associated with defects in Wnt, BMP and retinoic acid signaling (Hata et al. 104 2000, Huang et al. 2009, Casoni et al. 2020, Deshpande et al. 2020). Conditional Arl13b 105 or *Inpp5e* deletion in the SCPs results in their disorganization and thickening through 106 misregulation of ciliary PI3 kinase and AKT (Guo et al. 2019).

107 Ciliopathies are well established to be genetically complex. JSRD patients with 108 different ARL13B mutations can display distinct phenotypes, such as obesity in an 109 individual expressing ARL13B^{Y86C} and occipital encephalocele in a patient expressing 110 ARL13B^{R79Q} (Cantagrel *et al.* 2008; Thomas *et al.* 2015). This is further exemplified in 111 cases of related individuals carrying the same mutation but exhibiting different 112 phenotypes and even diagnoses. For example, JSRD-causing mutations in TMEM67

113 (R208X) and TMEM216 (R73H) can also cause the more severe disease Meckel 114 syndrome (Consugar et al. 2007; Otto et al. 2009; Valente et al. 2010). Understanding 115 the genetic modifiers and environmental contribution underlying the phenotypic variation 116 will be key to understanding disease etiology as will understanding when and how 117 relevant pathways interact. In mouse models of the JSRD- and Meckel Syndrome-linked 118 gene Tmem67, two phenotypic categories emerged: one with cerebellar malformations 119 resembling JSRD and another with more severe CNS defects reminiscent of Meckel 120 syndrome (Abdelhamed et al. 2013). The two categories correlated with whether cilia 121 were retained, with the severe Meckel-like phenotype observed in animals lacking cilia. 122 Furthermore, the two phenotypic groups impacted Hh and Wnt signaling differently, 123 pointing to both pathways being critical (Abdelhamed et al. 2019). Importantly, it is not 124 simply whether cilia are present, as another JSRD mouse model, *Talpid3*, lacks cilia yet 125 displays a JSRD-like small cerebellar vermis (Bashford and Subramanian 2019). Thus, 126 mouse models are incredibly informative yet point to the enormous complexity 127 underlying the MTS.

Here we investigate the role of ARL13B in relation to Hh signaling in two major features of the MTS: targeting of the SCPs to the thalamus and hypoplasia of the cerebellar vermis. We explore these processes using a series of mouse alleles through which we first define the roles of Hh signaling and ARL13B in SCP projections. Subsequently, we untangle the role of ARL13B from within and outside of the cilium and investigate a JS-causing patient allele. Taken together, our data illuminate the roles of ARL13B in MTS etiology and the complexity in modeling aspects of the MTS in mouse.

135

136 MATERIALS & METHODS

137 Mouse lines

138	All mice were cared for in accordance with NIH guidelines and Emory
139	University's Institutional Animal Care and Use Committee (IACUC). Lines used were
140	Nex-Cre (C3H-HeJ-Neurod6 ^{tm1(cre)Kan}) [MGI:2668659], Brn4-Cre (C3H/HeJ-Tg(Pou3f4-
141	cre)32Cren) [MGI:2158470], Smo ^{flox} (C3H/HeJ-Smo ^{tm2AMC}) [MGI:2176256], Arl13b ^{flox}
142	(C3H/HeJ-Arl13b ^{tm1Tc}) [MGI:4948239], Arl13b ^{V358A} (C57BL/6J-Arl13b ^{em1Tc})
143	[MGI:6256969], and <i>Arl13b^{R79Q}</i> (C57BL/6J- <i>Arl13b^{em2Tc}</i>) [MGI:6279301]. Note that
144	$ArI13b^{\Delta}$ is the deletion allele resulting from germline deletion of the conditional $ArI13b^{flox}$
145	allele. Genotyping was as previously described (Heydemann et al. 2001; Goebbels et
146	<i>al.</i> 2006; Nolan-Stevaux <i>et al.</i> 2009; Su <i>et al.</i> 2012; Gigante <i>et al.</i> 2020).
147	To generate the R79Q mutation in Arl13b, a CRISPR gRNA
148	(ATTATTATGCTGAATCCTATGG; PAM sequence is italicized) targeting exon 3 of the
149	Arl13b locus along with a 180bp donor oligo (5'-CTCCCACTGTTGGCTTTTCTAAAA-
150	TTGATCTGAGACAAGGAAAGTTCCAAGTTACCATCTTTGACTTAGGAGGTGGAAAA
151	AGAATTC <u>A</u> GGG <u>C</u> AT <u>A</u> TGGAAGAATTATTATGCTGAATCCTATGGGGTAATATTTGTT
152	GTGGATTCCAGTGATGAGGAGAGAATGGAAGAAACAAAGGAGA-3'; underlined
153	bases are engineered) were designed to generate a G-to-A change creating the R79Q
154	point mutation as well as A-to-C and T-to-A silent changes to create a Ndel restriction
155	site that could be used for genotyping (Millipore Sigma). The gRNA (50 ng/ul), ssDNA
156	oligo donor (50 ng/ul) and wild type Cas9 mRNA (10 ng/ul) were injected into 1-cell
157	C57BL/6J zygotes and subsequently transplanted at the 2-cell stage into C57BL/6J
158	pseudopregnant females by the Emory Transgenic and Gene Targeting Core; all

- 159 reagents were purchased from Millipore Sigma. Genomic DNA from toes was amplified
- 160 via PCR using primers (5'-TCACTTGCAACAGAGCATCC-3') and (5'-
- 161 ACAGCTCTGCCCGTGTTTAC-3') located upstream and downstream of the donor oligo
- 162 breakpoints; products were sequenced with the forward (first) primer. A single founder
- animal heterozygous for both the R79Q mutation and Ndel restriction site was identified
- 164 with no additional editing. Subsequent allele-specific genotyping of progeny was
- 165 performed on ear punch or yolk sac using the following primers: Fwd-wt primer: 5'-
- 166 GGAGGTGGAAAAAGAATaCg-3'; Fwd-mut primer: 5'-
- 167 gctctatggctgGGAGGTGGAAAAAGAATTga-3'; Rev primer: 5'-
- 168 AGTGCTAAGACACCCGAGGA-3'. PCR bands at 142bp (wild type) and/or 154bp
- 169 (mutant) were produced, due to the addition of 12 non-templated bases to the 5' end of
- 170 the Fwd-mut primer (lowercase). Note the 3' ends of the two forward primers differed in
- 171 the base that codes for the R to Q change (final nucleotide of the primer) and includes a
- 172 "wobble" base (lowercase) to provide allele-specific amplification after the first round of
- 173 PCR (Gaudet et al. 2009). In order to breed away any potential off-target edits, the
- 174 founder was backcrossed to C57BL/6J for three generations with at least two
- 175 independent meiotic opportunities for recombination in each generation.
- 176
- 177 Tract tracing injections and analysis

178 Tract tracing experiments were performed according to a protocol approved by 179 Emory University's Institutional Animal Care and Use Committee (IACUC). Male and 180 female mice at postnatal day 90 or older were used for tract tracing experiments. At 181 least 3 mice of each genotypic group were analyzed in experiments (exact N included in

Figures 1-3, S1). Mice were anesthetized with inhaled isoflurane and maintained under
anesthesia throughout the procedure. Animals were secured in the stereotax, and the
scalp was opened with bregma and lambda aligned to flatskull position. Dorsal thalamus
injections were targeted to the bregma (AP:-0.70, ML:+1.13, DV:-3.28, Angle:0°) and
ventral thalamus injections were targeted using coordinates to the bregma (AP:-0.70,
ML:-3.11, DV:-4.69, Angle:25°). Ventral injection targeting includes a 25° angle to avoid
pulling dye through the dorsal thalamus upon needle removal. Then, a 5 ul Hamilton
microsyringe was lowered to target and target was injected with lysine fixable dextran
tetramethylrhodamine neuroanatomical tracer (fluoro-Ruby, 10,000 MW, ThermoFisher
Scientific D1817). Animals received 0.05 - 0.5 ul injections of 10% dextran
tetramethylrhodamine in sterile phosphate buffered saline (PBS, pH = 7.25) unilaterally
at a rate of 0.1 ul/minute. The 0.5 ul injection volume initially used resulted in high
background (non-specific) fluorescence. Later surgeries were conducted with 0.05 ul of
dye, which resulted in lower background and retention of a strong signal in the DCN.
Seven days post-procedure, mice were perfused with 50mls of PBS followed by
30mls of 4% paraformaldehyde (PFA). Brains were kept in PFA overnight and
subsequently placed in 30% sucrose in 0.1M phosphate buffer (pH 7.3) for
cryoprotection for at least 48 hours. Brains were embedded in Tissue-Tek OCT
compound (Sakura) for coronal cryostat sectioning. Sections were 60 microns thick and
processed through 70% ethanol dehydration and 0.1% sudan black autofluorescence
quencher, rehydrated in PBS and treated with DAPI to stain nuclei prior to fluorescence
imaging. Images were taken on a Lionheart FX automated microscope (Biotek) or at 5x
magnification on a Leica DM6000B microscope (Leica) using SimplePCI imaging

205 software (Hamamatsu). The Leica images were subsequently stitched together to reveal 206 the entirety of the brain section in Fiji (Schindelin et al. 2012) or Photoshop (Adobe). 207 Surgical injection sites were assessed to ensure dye was present at the desired 208 injection site. If the injection was off-target or dye at the injection site was not seen, 209 samples were removed from analysis. Cerebellar images from injections were evaluated 210 for DCN staining with assessor blinded to genotype. The number of injections that resulted in fluorescent DCN for each injection site (dorsal and ventral thalamus) were 211 212 compared between mutant and control genotypes using a two-sided Fisher's exact test 213 (PRISM 8.2.0). 214 215 Phenotypic analysis of embryos 216 Timed matings of mice were performed to generate somite-matched embryos at 217 embryonic day 10.5 (E10.5). Embryos were dissected in cold PBS and processed for

immunofluorescence staining as previously described (Constable *et al.* 2020). Primary
antibodies used were: mouse anti-Shh (5E1, 1:10), mouse anti-Pax6 (PAX6, 1:100)
(Developmental Studies Hybridoma Bank), rabbit anti-Olig2 (AB9610, 1:500, Millipore
Sigma), and mouse anti-Arl13b (N295B/66, 1:1500, NeuroMab). Multiple sections from
three embryos of each genotype were examined.

223

224 Analysis of anatomical measures

Weanling age (P20-P24) male and female mice were sacrificed and brains were harvested and fixed in 4% PFA overnight at 4°. Ten sex-matched pairs of mouse brains were collected for each genotype; control animals were either wild type or heterozygous

228	for the <i>Arl13b</i> point mutation or floxed allele (so <i>Arl13b</i> ^{R79Q/+} , <i>Arl13b</i> ^{V358A/+} or <i>Arl13b</i> ^{flox/+})
229	or lacked Brn4-Cre (for Arl13b ^{Brn4-Cre}). Brains were imaged on a tilted stage to present a
230	surface view of the cerebellum, with a standard ruler in frame to confirm scale, using a
231	dissecting microscope (Leica MZFLIII). Measurements were made in FIJI (Schindelin et
232	al. 2012) with the investigator blind to genotype. Whole cerebellar width was measured
233	at the widest part of the cerebellum, coinciding with lobule CI or CII. Vermis width was
234	calculated by measuring the widest part of lobule VII (Deshpande et al. 2020).
235	Hemisphere and vermis heights were measured at the longest rostro-caudal point of the
236	hemisphere or at the midline of the vermis (see Figure 5). Body and brain weights were
237	measured on a standard lab scale. For each sex- and age-matched pair, the ratio of
238	mutant to control measures were calculated and graphed. A one-sample t-test was
239	performed after transforming the ratio data to a log(2) scale to normalize data
240	distribution (PRISM 8.2.0). Using the vermis width measures from our control brains
241	(mean = 2.6mm, SD = 0.18), a power calculation for a one-sided t-test estimated 90%
242	power to detect a 10% difference with 9-10 paired samples for a nominal alpha=0.05
243	(https://clincalc.com/stats/samplesize.aspx and
244	https://www.stat.ubc.ca/~rollin/stats/ssize/n2.html).

245

246 Data availability

Mouse lines are available upon request. Supplemental material available at figshare. Figure S1 contains diagrams illustrating the complete results of the injection and tract tracing experiments. Figure S2 contains a schematic of the CRISPR strategy.

The authors affirm that all data necessary for confirming the conclusions of the articleare present within the article and figures.

252

253 **RESULTS**

254 SMO is required for normal SCP projection to the dorsal thalamus

255 In order to test whether proper projection of SCPs requires Hh signaling, we 256 compared the SCP tracts in mice in which we deleted the gene encoding the obligate 257 Hh transducer, Smoothened (Smo), to control animals. As Smo null embryos die during 258 embryogenesis, we deleted Smo specifically in the projection neurons by generating Nex-Cre;Smo^{fl/fl} mice, which we refer to as Smo^{Nex-Cre} (Zhang et al. 2001; Caspary et al. 259 260 2002). Nex-Cre initiates CRE recombinase expression at E11.5, as the precursor cells 261 of the deep cerebellar nuclei (DCN) begin to migrate and become specified (Fink et al. 262 2006; Goebbels et al. 2006). In the mature cerebellum, the SCPs project rostrally from 263 the DCN (illustrated in Figure 1A). After entering the midbrain, the SCPs cross the 264 midline and again turn rostrally to project to two positions in the rostral thalamus: one 265 tract takes a slight dorsal path and the other tract remains in the same plane; for 266 simplicity here, we term these projection sites the dorsal and ventral thalamus, 267 respectively (Bohne et al. 2019). To examine the SCP tracts, we used retrograde tract 268 tracing in which we performed stereotaxic injections of a lipophilic dextran dye into 269 either the dorsal (Figure 1B) or ventral (Figure 1C) thalamus and allowed the dye to 270 diffuse through the axons to the associated neuron's cell body (~7 days); we then 271 sacrificed the animal and examined the cerebellum for evidence of the lipophilic dye 272 indicating tracing.

273 We found that both dorsal and ventral thalamus injections resulted in visible 274 clusters of dye-stained cells in the contralateral DCN, and not the ipsilateral DCN, in 275 control animals indicating the retrograde tract tracing reliably labelled the SCPs in our hands (Figures 1D-E, S1A-B, dorsal: 6/8; ventral: 8/11). In the Smo^{Nex-Cre} mice, the 276 277 results differed depending on whether we injected in the dorsal or ventral thalamus 278 (Figures 1F-G, S1C-D). In the ventral thalamus injections, we detected dye-stained 279 clusters of cells in the contralateral DCN but not the ipsilateral DCN, indicating normal 280 SCP projection to the ventral thalamus (Figure 1G, 4/4 injections). This indicates that at 281 least some SCPs cross the midline. In the dorsal thalamus injections, we could not 282 detect dye-stained clusters of cells in either the contralateral or ipsilateral DCN (Figure 283 1F, 0/6 injections) suggesting that SCPs lacking SMO do not project to the dorsal 284 thalamus. These data implicate SMO as critical for proper projection of the SCPs to the 285 dorsal thalamus.

286

287 ARL13B is required for normal SCP projection to the dorsal thalamus

288 Given that ARL13B regulates vertebrate Hh signaling in a variety of contexts, we 289 next assessed ARL13B's role in proper SCP projection. In order to delete ARL13B 290 specifically in projection neurons, we generated Nex-Cre;Arl13b^{fl/fl} mice, which we refer to as Arl13b^{Nex-Cre}. We performed dorsal and ventral thalamus injections for retrograde 291 292 tract tracing to examine the SCPs (Figures 1H-I, S1C-D). In the ventral thalamus injections of Arl13b^{Nex-Cre} mice, we found dye-stained clusters of cells in the 293 294 contralateral DCN consistent with normal SCP projections crossing the midline and 295 projecting to the ventral thalamus (Figure 1I, 4/4 injections). In contrast, in the dorsal

thalamus injections of *Arl13b^{Nex-Cre}* mice, we generally did not detect dye-stained
clusters of cells in either the contralateral or ipsilateral DCN, suggesting that the SCPs
lacking ARL13B do not project to the dorsal thalamus (Figure 1H, 1/7 injections). These
data link ARL13B function to normal SCP projection. Furthermore, they reveal a similar
phenotype in *Smo^{Nex-Cre}* and *Arl13b^{Nex-Cre}* mice.

301

302 ARL13B does not function from within cilia to mediate SCP guidance

303 ARL13B and the other 35 genes implicated in Joubert syndrome associate with 304 the cilium or centrosome leading to the assumption that protein dysfunction from these 305 locales underlies JSRD phenotypes (Parisi 2019). To directly ask whether ARL13B 306 mediates SCP guidance to the dorsal thalamus from within cilia, we examined a mouse expressing a cilia-excluded variant of ARL13B, ARL13B^{V358A} (Figure 2) (Gigante et al. 307 2020). We previously demonstrated that ARL13B^{V358A} retains all known ARL13B 308 309 biochemical activity, is undetectable in cilia yet transduces vertebrate Hh signaling 310 normally (Mariani et al. 2016; Gigante et al. 2020). We found that either dorsal or ventral 311 thalamus injections resulted in visible clusters of dye-stained cells in the contralateral DCN in control (Figures 2A-B, S1G-H, dorsal: 3/3; ventral: 4/4) and Arl13b^{V358A/V358A} 312 313 (Figure 2C-D, dorsal: 4/4; ventral: 3/3) animals. In the context of the previous result showing that Arl13b^{Nex-Cre} mice display abnormal SCP projections to the dorsal 314 315 thalamus, these data demonstrate that ARL13B does not function from within cilia to 316 regulate SCP projections.

317

318 SCP projection is normal in mice expressing a Joubert-causing allele, Arl13b^{R79Q}

319	In order to understand the relationship between ARL13B and MTS formation in
320	Joubert syndrome, we generated a mouse expressing the JSRD-causing R79Q
321	mutation (Figure 3A). We used CRISPR/Cas9 editing to change the conserved residue
322	in the mouse genome (Figures 3B, S2). This amino acid change disrupts ARL13B's
323	GEF activity for ARL3 (Gotthardt et al. 2015; Ivanova et al. 2017). We found
324	Arl13b ^{R79Q/R79Q} mice were viable and fertile. We bred the Arl13b ^{R79Q} allele to the null
325	<i>Arl13b</i> ^{Δ} allele to make <i>Arl13b</i> ^{<i>R79Q/Δ</i> animals, which we found survived to adulthood. As}
326	<i>Arl13b</i> ^{Δ/Δ} are embryonic lethal, this genetically demonstrates that <i>Arl13b</i> ^{<i>R79Q</i>} is a
327	hypomorphic allele of ARL13B (Su et al. 2012).
328	To assess the role of ARL13B ^{R79Q} in SCP guidance, we performed dorsal and
329	ventral thalamus dye injections in control and Arl13b ^{R79Q/R79Q} mice. We identified visible
330	clusters of dye-stained cells in the contralateral DCN in control (Figures 3C-D, S1E-F,
331	dorsal: 4/4; ventral: 3/3) and <i>Arl13b</i> ^{R79Q/R79Q} (Figure 3E-F, dorsal: 3/3; ventral: 3/4)
332	animals. Thus, despite the constitutive expression of the JSRD-causing allele
333	throughout development, we did not detect a SCP projection defect in the
334	Arl13b ^{R79Q/R79Q} mouse model. In the context of the abnormal SCP projections to the
335	dorsal thalamus that we identified in the Smo ^{Nex-Cre} and Arl13b ^{Nex-Cre} mice, this result
336	indicates that the <i>Arl13b</i> ^{R79Q} allele does not disrupt SMO function or any ARL13B
337	function that regulates SMO.
338	
220	AutophR790/R799 miss display power Chla signal transductions in power tube pottomics

ArI13b^{R79Q/R79Q} mice display normal Shh signal transduction in neural tube patterning
 To further investigate the role of the ArI13b^{R79Q} allele in Hh signaling, we
 examined embryonic neural patterning as it is exquisitely sensitive to alterations in Shh

342 activity (Chiang et al. 1996; Briscoe and Ericson 1999). We generated E10.5 embryos 343 and stained neural tube sections with antibodies against Shh. Olig2 and Pax6 (Figure 344 4). As expected in wild type embryos, we observed Shh expression in the ventral-most 345 cells (the floorplate), Olig2 expression in lateral cells and Pax6 expression dorsally. We also saw the established abnormal cell fates in null $Arl13b^{\Delta/\Delta}$ embryos: loss of Shh 346 staining in the floorplate (Figure 4D), dorsal and ventral expansion of Olig2 expression 347 348 (Figure 4H), and a dorsal shift in Pax6 expression (Figure 4L) (Su et al. 2012). We found both *Arl13b*^{R79Q/R79Q} (Figure 4B, F, J) and *Arl13b*^{R79Q/Δ} (Figure 4C, G, K) embryos 349 350 displayed neural patterning indistinguishable from wild type embryos, indicating the 351 *Arl13b*^{*R79Q}</sup> allele is not dosage-sensitive and does not disrupt Shh signaling in*</sup> determining neural cell fate. In addition, ARL13B^{R79Q} protein localized to cilia (Figure 352 353 4N), consistent with previous results (Li et al. 2010; Humbert et al. 2012; Li et al. 2016; 354 Mariani et al. 2016).

355

356 Arl13b^{R79Q/R79Q} mice display normal cerebellar width

The lack of a SCP projection phenotype in the Arl13b^{R79Q/R79Q} mice surprised us 357 358 since JS patients display the MTS. In addition to defects in the SCPs, the MTS is due to 359 an underdeveloped cerebellar vermis, so we examined the width of the cerebellum and 360 the cerebellar vermis (Figure 5) (Aguilar et al. 2012). To quantify cerebellar width, we 361 performed analysis of surface-facing anatomical measurements validated to be 362 sufficiently sensitive to detect small differences in vermis width (Deshpande et al. 2020). 363 Briefly, we measured cerebellar width as well as cerebellar vermis width (widest part of 364 lobule VII) of fixed whole mount dissected brains. For each sex- and age-matched pair,

we calculated the ratio of the width measurements from mutant to control, which we compared to a hypothetical value of 1 (indicating no difference between groups). We detected no differences in the overall cerebellar width or the cerebellar vermis width between control and $Arl13b^{R79Q/R79Q}$ mice of either sex (Figure 5B). Furthermore, we found no difference in body or brain weight for $Arl13b^{R79Q/R79Q}$ mutants compared to controls (Figure 5B). Thus, unlike patients carrying $ARL13B^{R79Q/R79Q}$, $Arl13b^{R79Q/R79Q}$ mice do not display a detectable growth deficit in the cerebellar vermis.

372

373 Global cerebellar hypoplasia is observed in mice lacking Ar13b in all neurons

374 Cerebellar size is well established to be regulated, in part, via Shh signaling 375 which controls proliferation of the cerebellar granule precursor cells (Kenney and 376 Rowitch 2000; Chizhikov et al. 2007). In order to better understand the vermis 377 hypoplasia phenotype seen in JBTS patients in relation to ARL13B, we wanted to 378 investigate how ARL13B regulates cerebellar width. To do so, we crossed the Brn4-Cre allele into the conditional null Arl13b^{fl/fl} background, called Arl13b^{Brn4-Cre} (Figure 6). Brn4-379 380 Cre initiates expression at E8.5 throughout the neuroectoderm so the cerebellum 381 develops in the absence of ARL13B (Heydemann et al. 2001; Hazen et al. 2012). We 382 again calculated width ratios using surface-facing anatomical measurements and found 383 the overall width of the cerebellum was 6% reduced in both females and males lacking 384 ARL13B compared to control littermates at weaning (Figure 6B, p<0.1). More striking, in 385 the cerebellar vermis we detected a 27% reduction in width in female and a 33% reduction in male mutants compared to controls (Figure 6B, p<0.0001). ArI13b^{Brn4-Cre} 386 387 mice develop hydrocephaly just after weaning which often leads to death. This is

reflected in the body and brain weight ratios: while the mutant mice had slightly lower
 body weights, they had comparatively heavier brains (Figure 6B). From these data, we

390 conclude that loss of ARL13B leads to a modest global cerebellar width deficit and a

391 more pronounced cerebellar vermis width reduction.

- 392
- 393 Arl13b^{V358A/V358A} mice display normal cerebellar width

JS is classified as a ciliopathy due to the majority of causative genes encoding proteins that, like ARL13B, are associated with cilia. In order to better understand the role of ciliary ARL13B in cerebellar size, we examined cerebellar width in the mice expressing the cilia-excluded variant ARL13B^{V358A} (Figure 7) (Gigante *et al.* 2020). We detected no difference in the overall cerebellar width or that of the cerebellar vermis between control and *Arl13b^{V358A/V358A}* mice (Figure 7B). Thus, ARL13B does not control cerebellar width from within cilia.

401

402 **DISCUSSION**

403 Here we demonstrate that complete loss of *Arl13b* function in mouse can account 404 for two aspects of the MTS: aberrant SCP thalamic targeting and cerebellar vermis 405 hypoplasia. We expand the role of Hh signaling as a critical guidance cue by showing it 406 is required for proper SCP projection to the dorsal thalamus. Our finding that the SCP phenotype is similar in Smo^{Nex-Cre} and Arl13b^{Nex-Cre} mice is consistent with a model 407 408 whereby ARL13B regulates SCP projections to the dorsal thalamus via a SMO-409 dependent mechanism. In line with previous work showing that ARL13B does not 410 function from within cilia to regulate Shh-guided axon guidance, we found normal SCP

411 thalamic targeting in mice expressing only a cilia-excluded ARL13B variant (Ferent *et al.* 412 2019). By mutating a conserved arginine to glutamine, we generated a mouse 413 expressing a mutation linked to JSRD in humans and observed no change in vertebrate 414 Hh signaling (Cantagrel *et al.* 2008). Additionally, we identified no defects in 415 $Arl13b^{R79Q/R79Q}$ SCP projections. Whereas complete ARL13B deletion ($Arl13b^{Bm4-Cre}$) in 416 the cerebellum led to global hypoplasia, we show the cerebellum of $Arl13b^{R79Q/R79Q}$ mice 417 is not significantly different in width compared to controls.

418 Overall, our data indicate ARL13B function is critical for both SCP targeting and 419 controlling cerebellar vermis width. At one level, our data implicate Hh signaling in the 420 etiology of the MTS since we show that SCP targeting requires SMO. However, at 421 another level, our data indicate that Hh-independent pathways are at play as we don't 422 observe Hh-dependent neural tube patterning defects in the presence of the JSRDcausing *Arl13b*^{R79Q} allele. In other mouse models of JSRD where the hypoplasia is 423 424 specific to the cerebellar vermis, Wht signaling is affected (Lancaster et al. 2011). Thus, 425 the MTS could be due to disruption of different pathways in the SCPs and the vermis. 426 This would imply that the 35 JSRD implicated genes all affect the distinct pathways in a 427 similar manner (Parisi 2019). Alternatively, the MTS may form due to alterations in any 428 of a few pathways – and it is even possible that alterations in one pathway could impact 429 other pathways – or the ability of cells to respond to those other pathways. Such a 430 model is hinted at by previous work showing interplay between the Hh and Wnt 431 pathways underlying the severity of hindbrain phenotypes (Hagemann and Scholpp 432 2012; Bashford and Subramanian 2019). While we haven't detected any changes in 433 What response in the absence of ARL13B function, we may have not examined the

relevant biological process or used a sensitive enough readout (Horner and Caspary
2011). Parallel reasoning would thus suggest that while *Arl13b*^{*R79Q/R79Q*} mice clearly
transduce Hh reasonably well, there may be subtle changes in Shh signaling or
changes that influence Wnt signaling. Our data are consistent with the complexity
exhibited by other JSRD mouse models examined to date (Delous *et al.* 2007; GarciaGonzalo *et al.* 2011; Roberson *et al.* 2015; Bashford and Subramanian 2019).

440 In patients, the SCP targeting deficit appears more severe than what we 441 observed in the mice. Available methods for live-imaging and examination of post-442 mortem tissues suggest a range of SCP decussation defects, with some tracts 443 appearing thickened on the ipsilateral side relative to their DCN (Yachnis and Rorke 444 1999; Poretti et al. 2007). Surprisingly, in the mutant mice we infer midline crossing of the SCPs. In the case of the Smo^{Nex-Cre} conditional mice, it is formally possible that the 445 446 SCPs do not rely on SMO for midline crossing but only for subsequent targeting to the dorsal thalamus. The fact that the Arl13b^{Nex-Cre} conditional mice display a highly similar 447 448 phenotype to the Smo^{Nex-Cre} conditional mice makes this less likely, since ARL13B is 449 directly implicated in JSRD and regulates SMO-dependent axon guidance in other 450 contexts (Cantagrel et al. 2008; Ferent et al. 2019). It is also plausible that the protein 451 turnover driven by Nex-Cre completed after midline crossing occurred. Nex-Cre 452 expression initiates at E11.5 in the cells on the rhombic lip of the cerebellar anlage as 453 they start to migrate and be specified before occupying the deep cerebellar nuclei (Fink 454 et al. 2006; Goebbels et al. 2006). We expect deletion would occur in the precursors 455 and therefore the neurons of the DCN would not express protein. Finally, it is possible 456 that the mouse is not a valid system in which to model the SCP midline crossing defect.

This might explain why we saw no defects in the SCP targeting of the Arl13b^{R79Q/R79Q} 457 458 mice, as this is a constitutive mutation that requires no protein turnover, yet homozygous expression of ARL13B^{R79Q} in patients results in the molar tooth sign, which 459 has been associated with failed decussation of white matter tracts (Quisling et al. 1999). 460 461 Indeed, other mouse mutants such as Cep290 and Ahi1 which recapitulate the 462 cerebellar vermis hypoplasia, also do not display midline crossing defects in the SCPs (Lancaster et al. 2011). Whether this is due to anatomical distinctions between the 463 464 cerebellum in mouse and human or the genetic background on which these models 465 were examined are open questions. Recent work highlights clear molecular and 466 temporal differences between mouse and human cerebellar development (Haldipur et 467 al. 2019; Behesti et al. 2021).

Examining SCP projections is labor intensive and it has not been done 468 469 systematically among the JSRD mouse models (Bashford and Subramanian 2019; Guo et al. 2019). While previous work showed that Arl13b^{Nex-Cre} and Inpp5e^{Nex-Cre} mice 470 exhibit SCP targeting deficits, here we pinpoint the Arl13b^{Nex-Cre} defect as specific to the 471 472 projection to the dorsal thalamus (Guo et al. 2019). The projection to the ventral 473 thalamus remains intact, suggesting there is not a generalized deficit in axon outgrowth within the tract. The work on the Arl13b^{Nex-Cre} and Inpp5e^{Nex-Cre} SCP targeting deficits 474 475 argue that PI3K/Akt signaling from within cilia led to the tract defects (Guo et al. 2019). 476 However, we found that cilia-excluded ARL13B mediated SCP targeting normally. 477 These conflicting results could be explained by differences in the experimental details 478 as the data supporting ciliary ARL13B function used a human ARL13B viral expression 479 construct to rescue conditionally-deleted mice whereas we used genetic mutations

engineered at the endogenous locus in this study. Alternatively, these data could
indicate that ARL13B plays an important cellular role in the ciliary trafficking of key
components needed for the PI3K/Akt pathways.

483 JSRD-causing mutations in ARL13B are generally restricted to the GTPase 484 domain of the protein, although two residues outside that domain are implicated in 485 disease (Cantagrel et al. 2008; Bachmann-Gagescu et al. 2015; Thomas et al. 2015; 486 Shaheen et al. 2016; Rafiullah et al. 2017). Based on other ARL proteins, ARL13B likely 487 assumes distinct conformations upon the binding either GDP or GTP, permitting 488 different binding partners or altering affinities for binding partners (Pasgualato et al. 489 2002; Miertzschke et al. 2014). None of the tested JSRD-causing mutations (R79Q, 490 Y86C or R200C) disrupt GTP binding or hydrolysis, however, all three mutations disrupt 491 ARL13B function as an ARL3 GEF (Ivanova et al. 2017). The arginine at this position is 492 located within the Switch 2 region of ARL13B and is conserved in humans, mice, 493 zebrafish and Chlamydomonas (Figure 3B). We were surprised that we were unable to 494 detect any defects in our mouse, as we expected to model some aspect of Joubert 495 syndrome. Humans with homozygous R79Q mutation exhibit motor and ocular defects 496 (among other symptoms), whereas arl13b-null zebrafish injected with human ARL13B-497 R79Q mRNA only partially rescue the ciliopathy phenotypes of curved body axis and 498 cystic kidney (Cantagrel et al. 2008). These species-dependent differences emphasize 499 the importance of analyzing mutations expressed from the endogenous promoter over 500 the course of normal development. A recent study linked arl13b disruption during 501 zebrafish development to reduced granule and Purkinje cells through a down-regulation 502 of Wnt signaling (Zhu et al. 2020). Given that complete deletion of ARL13B impacts

- 503 broader biological processes in the cerebellum than the R79Q mutation and that the null
- 504 mutant misregulates Hh signaling whereas R79Q does not, we conclude that a subset
- 505 of ARL13B function is disrupted in JSRD.
- 506

507 Acknowledgements

- 508 We are grateful to L. Mariani for her initial work on this project, R.E. Van Sciver and E.
- 509 Gigante for critical comments on the manuscript and J.G. Mulle for the statistical
- 510 consults.
- 511

512 Funding

- 513 This work was supported by funding from National Institutes of Health grants
- 514 R01NS090029, R01GM110663 and R35GM122549 to T.C. and T32GM008490 and
- 515 F31NS101806 to S.K.S. with additional support from the Emory University Integrated
- 516 Cellular Imaging Microscopy Core of the Emory Neuroscience NINDS Core Facilities
- 517 grant, P30NS055077. This study was supported in part by the Mouse Transgenic and
- 518 Gene Targeting Core (TMF), which is subsidized by the Emory university School of
- 519 Medicine and is one of the Emory Integrated Core Facilities. Additional support was
- 520 provided by the National Center for Advancing Translational Sciences of the National
- 521 Institutes of Health under Award Number UL1TR000454. The content is solely the
- 522 responsibility of the authors and does not necessarily reflect the official views of the
- 523 National Institutes of Health
- 524

525 Conflicts of Interest

- 526 The authors have no competing interests to declare.
- 527

528 Author contributions statement

- 529 Author Contributions: Conceptualization T.C.; Methodology S.K.S. and A.B.L.;
- 530 Validation S.K.S. and A.B.L; Formal Analysis S.K.S. and A.B.L.; Investigation S.K.S.
- and A.B.L.; Writing Original Draft S.K.S. and T.C.; Writing Review & Editing S.K.S.,
- 532 A.B.L. and T.C.; Visualization S.K.S. and A.B.L.; Supervision T.C.; Project
- 533 Administration T.C.; Funding Acquisition T.C.
- 534

535 **References**

- 536 Abdelhamed, Z. A., D. I. Abdelmottaleb, M. E. El-Asrag, S. Natarajan, G. Wheway et al.,
- 537 2019 The ciliary Frizzled-like receptor Tmem67 regulates canonical Wwnt/beta-
- 538 catenin signalling in the developing cerebellum via Hoxb5. *Sci Rep.* **9:** 5446.
- 539 doi:10.1038/s41598-019-41940-5
- 540 Abdelhamed, Z. A., G. Wheway, K. Szymanska, S. Natarajan, C. Toomes et al., 2013
- 541 Variable expressivity of ciliopathy neurological phenotypes that encompass
- 542 Meckel-Gruber syndrome and Joubert syndrome is caused by complex de-
- 543 regulated ciliogenesis, Shh and Wnt signalling defects. *Hum Mol Genet.* 22:
- 544 1358-1372. doi:10.1093/hmg/dds546
- 545 Aguilar, A., A. Meunier, L. Strehl, J. Martinovic, M. Bonniere et al., 2012 Analysis of
- 546 human samples reveals impaired SHH-dependent cerebellar development in
- 547 Joubert syndrome/Meckel syndrome. *Proc Natl Acad Sci U S A.* **109:** 16951-
- 548 16956. doi:10.1073/pnas.1201408109

549	Alkanderi, S., E. Molinari, R. Shaheen, Y. Elmaghloob, L. A. Stephen et al., 2018 ARL3
550	mutations cause Joubert syndrome by disrupting ciliary protein composition. Am
551	<i>J Hum Genet.</i> 103: 612-620. doi:10.1016/j.ajhg.2018.08.015
552	Arts, H. H., D. Doherty, S. E. C van Beersum, M. A. Parisi, S. J. F. Letteboer et al., 2007
553	Mutations in the gene encoding the basal body protein RPGRIP1L, a
554	nephrocystin-4 interactor, cause Joubert syndrome. Nat Genet. 39: 882-888.
555	doi:10.1038/ng2069
556	Asadollahi, R., J. E. Strauss, M. Zenker, O. Beuing, S. Edvardson et al., 2018 Clinical
557	and experimental evidence suggest a link between KIF7 and C5orf42-related
558	ciliopathies through Sonic Hedgehog signaling. Eur J Hum Genet. 26: 197-209.
559	doi:10.1038/s41431-017-0019-9
560	Bachmann-Gagescu, R., J. C. Dempsey, I. G. Phelps, B. J. O'Roak, D. M. Knutzen et
561	al., 2015 Joubert syndrome: A model for untangling recessive disorders with
562	extreme genetic heterogeneity. J Med Genet. 52: 514-522.
563	doi:10.1136/jmedgenet-2015-103087
564	Bachmann-Gagescu, R., J. C. Dempsey, S. Bulgheroni, M. L. Chen, S. D'Arrigo et al.,
565	2020 Healthcare recommendations for Joubert syndrome. Am J Med Genet A.
566	182: 229-249. doi:10.1002/ajmg.a.61399
567	Bashford, A. L., and V. Subramanian, 2019 Mice with a conditional deletion of Talpid3
568	(KIAA0586) - a model for Joubert syndrome. J Pathol. 248: 396-408.
569	doi:10.1002/path.5271
570	Bay, S.N., A. B. Long, and T. Caspary, 2018 Disruption of the ciliary GTPpase Arl13b
571	suppresses Sonic hedgehog overactivation and inhibits medulloblastoma

572 formation. *Proc Natl Acad Sci U S A*. **115**: 1570-1575.

573 doi:10.1073/pnas.1706977115

- 574 Behesti, H. A. Kocabas, D. E. Buchholz, T. S. Carroll, and M. E. Hatten, 2021 Altered
- 575 temporal sequence of transcriptional regulators in the generation of human
- 576 cerebellar granule cells. bioRxiv. doi:10.1101/2021.01.17.427030 (Preprint
- 577 posted January 17, 2021).
- 578 Bielas, S. L., J. L. Silhavy, F. Brancati, M. V. Kisseleva, L. Al-Gazali et al., 2009
- 579 Mutations in INPP5E, encoding inositol polyphosphate-5-phosphatase E, link
- 580 phosphatidyl inositol signaling to the ciliopathies. *Nat Genet.* **41:** 1032-1036.
- 581 doi:10.1038/ng.423
- 582 Bimonte, S., A. De Angelis, L. Quagliata, F. Giusti, R. Tammaro et al., 2011 Ofd1 is
- 583 required in limb bud patterning and endochondral bone development. *Dev Biol.*

584 **349:** 179-191. doi:10.1016/j.ydbio.2010.09.020

- 585 Bohne, P., M. K. Schwarz, S. Herlitze, and M. D. Mark, 2019 A new projection from the
- 586 deep cerebellar nuclei to the hippocampus via the ventrolateral and laterodorsal
- 587 thalamus in mice. *Front Neural Circuits*. **13**: 51. doi:10.3389/fncir.2019.00051
- 588 Brancati, F., B. Dallapiccola, and E. M. Valente, 2010 Joubert syndrome and related 589 disorders. *Orphanet J Rare Dis.* **5:** 20. doi:10.1186/1750-1172-5-20
- 590 Breslow, D. K., S. Hoogendoorn, A. R. Kopp, D. W. Morgens, B. K. Vu et al., 2018 A
- 591 CRISPR-based screen for Hedgehog signaling provides insights into ciliary
- 592 function and ciliopathies. *Nat Genet.* **50:** 460-471. doi:10.1038/s41588-018-0054-
- 593

- 594 Briscoe, J., and J. Ericson J, 1999 The specification of neuronal identity by graded
- 595 Sonic Hedgehog signalling. *Semin Cell Dev Biol.* **10:** 353-362.
- 596 doi:10.1006/scdb.1999.0295
- 597 Cantagrel, V., J. L. Silhavy, S. L. Bielas, D. Swistun, S. E. Marsh et al., 2008 Mutations
- 598 in the cilia gene ARL13B lead to the classical form of Jjoubert syndrome. *Am J*
- 599 *Hum Genet.* **83:** 170-179. doi:10.1016/j.ajhg.2008.06.023
- 600 Casoni, F., L. Croci, F. Vincenti, P. Podini, M. Riba et al., 2020 ZFP423 regulates early
- 601 patterning and multiciliogenesis in the hindbrain choroid plexus. *Development*.
- 602 **147:** dev190173. doi:10.1242/dev.190173
- 603 Caspary, T., M. J. Garcia-Garcia, D. Huangfu, J. T. Eggenschwiler, M. R. Wyler et al.,
- 604 2002 Mouse Dispatched homolog1 is required for long-range, but not juxtacrine,
- 605 Hh signaling. *Curr Biol.* **12:** 1628-1632. doi:10.1016/s)960-9822(02)01147-8
- 606 Caspary, T., C. E. Larkins, and K. V. Anderson, 2007 The graded response to Sonic
- 607 Hedgehog depends on cilia architecture. *Dev Cell.* **12**: 767-778.
- 608 doi:10.1016/j.devcel.2007.03.004
- 609 Charron, F., E. Stein, J. Jeong, A. P. McMahon, and M. Tessier-Lavigne, 2003 The
- 610 morphogen sonic hedgehog is an axonal chemoattractant that collaborates with
- 611 netrin-1 in midline axon guidance. *Cell.* **113:** 11-23. doi:10.1016/s0092-
- 612 8674(03)00199-5
- 613 Chavez, M., S. Ena, J. Van Sande, A. de Kerchove d'Exaerde, S. Schurmans et al.,
- 614 2015 Modulation of ciliary phosphoinositide content regulates trafficking and
- 615 Sonic hedgehog signaling output. *Dev Cell.* **34:** 338-350.
- 616 doi:10.1016/j.devcel.2015.06.016

- 617 Chiang, C., Y. Litingtung, E. Lee, K. E. Young, J. L. Corden et al., 1996 Cyclopia and
- 618 defective axial patterning in mice lacking Ssonic hedgehog gene function.
- 619 *Nature.* **383:** 407-413. Doi:10.1038/383407a0
- 620 Chih, B., P. Liu, Y. Chinn, C. Chalouni, L. G. Komuves et al., 2011 A ciliopathy complex
- 621 at the transition zone protects the cilia as a privileged membrane domain. *Nat*
- 622 Cell Biol. 14: 61-72. doi:10.1038/ncb2410
- 623 Chizhikov, V. V., J. Davenport, Q. Zhang, E. K. Shih, O. A. Cabello et al., 2007 Cilia
- 624 proteins control cerebellar morphogenesis by promoting expansion of the granule
- 625 progenitor pool. *J Neurosci.* **27:** 9780-9789. doi:10.1523/JNEUROSCI.5586-
- 626 06.2007
- 627 Christopher, K. J., B. Wang, Y. Kong, and S. D. Weatherbee, 2012 Forward genetics
- 628 uncovers Transmembrane protein 107 as a novel factor required for ciliogenesis

and Sonic hedgehog signaling. *Dev Biol.* **368:** 382-392.

- 630 doi:10.1016/j.ydbio.2012.06.008
- 631 Constable, S., A. B. Long, K. A. Floyd, S. Schurmans, and T. Caspary, 2020 The ciliary
- 632 phosphatidylinositol phosphatase Inpp5e plays positive and negative regulatory
- 633 roles in Shh signaling. *Development.* **147:** dev183301. doi:10.1242/dev.183301
- 634 Consugar, M. B., V. J. Kubly, D. J. Lager, C. J. Hommerding, W. C. Wong et al., 2007
- 635 Molecular diagnostics of Meckel–Gruber syndrome highlights phenotypic
- differences between MKS1 and MKS3. *Hum Genet.* **121:** 591-599.
- 637 doi:10.1007/s00439-007-0341-3
- Dahmane, N., and A. Ruiz i Altaba, 1999 Sonic hedgehog regulates the growth and
 patterning of the cerebellum. *Development.* **126**: 3089-3100.

- Davey, M. G., I. R. Paton, Y. Yin, M. Schmidt, F. K. Bangs et al., 2006 The chicken
- talpid3 gene encodes a novel protein essential for Hedgehog signaling. *Genes*
- 642 *Dev.* **20:** 1365-1377. doi:10.1101/gad.369106
- 643 Delous, M., L. Baala, R. Salomon, C. Laclef, J. Vierkotten et al., 2007 The ciliary gene
- 644 RPGRIP1L is mutated in cerebello-oculo-renal syndrome (Joubert syndrome type
- 645 B) and Meckel syndrome. *Nat Genet.* **39:** 875-881. doi:10.1038/ng2039
- 646 Deshpande, O., R. Z. Lara, O. R. Zhang, D. Concepcion, and B. A. Hamilton, 2020
- 647 ZNF423 patient variants, truncations, and in-frame deletions in mice define an
- 648 allele-dependent range of midline brain abnormalities. *PLoS Genet.* **16**:
- 649 e1009017. doi:10.1371/journal.pgen.1009017
- Doherty, D., 2009 Joubert syndrome: Insights into brain development, cilium biology,

and complex disease. *Semin Pediatr Neurol.* **16:** 143-154.

652 doi:10.1016/j.spen.2009.06.002

- Dowdle, W. E., J. F. Robinson, A. Kneist, M. S. Sirerol-Piquer, S. G. M. Frints et al.,
- 654 2011 Disruption of a ciliary B9 protein complex causes Meckel syndrome. Am J

655 *Hum Genet.* **89:** 94-110. doi:10.1016/j.ajhg.2011.06.003

656 Ferent, J., S. Constable, E. D. Gigante, P. T. Yam, L. E. Mariani et al., 2019 The ciliary

657 protein Arl13b functions outside of the primary cilium in Shh-mediated axon

658 guidance. *Cell Rep.* **29:** 3356-3366.e3353. doi:10.1016/j.celrep.2019.11.015

- Fink, A. J., C. Englund, R. A. M. Daza, D. Pham, C. Lau et al., 2006 Development of
- the deep cerebellar nuclei: Transcription factors and cell migration from the
- 661 rhombic lip. *J Neurosci.* **26:** 3066-3076. doi:10.1523/JNEUROSCI.5203-05.2006

- 662 Frikstad, K-A. M., E. Molinari, M. Thoresen, S. A. Ramsbottom, F. Hughes et al., 2019
- 663 A CEP104-CSPP1 complex is required for formation of primary cilia competent in
- 664 Hedgehog signaling. *Cell Rep.* **28:** 1907-1922.e6
- 665 doi:10.1016/j.celrep.2019.07.025
- 666 Garcia-Gonzalo, F. R., K. C. Corbit, M. S. Sirerol-Piquer, G. Ramaswami, E. A. Otto et
- al., 2011 A transition zone complex regulates mammalian ciliogenesis and ciliary
 membrane composition. *Nat Genet.* 43: 776-784. doi:10.1038/ng.891
- 669 Garcia-Gonzalo, F. R., S. C. Phua, E. C. Roberson, G. Garcia 3rd, M. Abedin et al.,
- 670 2015 Phosphoinositides regulate ciliary protein trafficking to modulate Hedgehog
- 671 signaling. *Dev Cell.* **34:** 400-409. doi:10.1016/j.devcel.2015.08.001
- Gaudet, M., A-G. Fara, I. Beritognolo, and M. Sabatti, 2009 Allele-specific PCR in SNP
 genotyping. *Methods Mol Biol.* 578: 415-424. doi:10.1007/978-1-60327-411-1 26
- Gigante, E. D., M. R. Taylor, A. A. Ivanova, R. A. Kahn, and T. Caspary, 2020. ARL13B
- 675 regulates Sonic hedgehog signaling from outside primary cilia. *eLife.* **9**: e50434.
- 676 doi:10.7554/eLife.50434
- 677 Goebbels, S., I. Bormuth, U. Bode, O. Hermanson, M. H. Schwab et al., 2006 Genetic
- targeting of principal neurons in neocortex and hippocampus of NEX-Cre mice.
- 679 *Genesis.* **44:** 611-621. doi:10.1002/dvg.20256
- 680 Gotthardt, K., M. Lokaj, C. Koerner, N. Falk, A. Giessl et al., 2015 A G-protein
- 681 activation cascade from Arl13b to Arl3 and implications for ciliary targeting of
- 682 lipidated proteins. *eLife*. **4**: e11859. doi:10.7554/eLife.11859

683	Guo, J., J. M. Otis, S. K. Suciu, C. Catalano, L. Xing et al., 2019 Primary cilia signaling
684	promotes axonal tract development and is disrupted in Joubert syndrome-related
685	disorders models. Dev Cell. 51: 759-774 e755. doi:10.1016/j.devcel.2019.11.005
686	Hagemann, A. I. H., and S. Scholpp, 2012 The tale of the three brothers – Shh, Wnt,
687	and Fgf during development of the thalamus. Front Neurosci. 6: 76.
688	doi:10.3389/fnins.2012.00076
689	Haldipur, P., K. A. Aldinger, S. Bernardo, M. Deng, A. E. Timms et al., 2019
690	Spatiotemporal expansion of primary progenitor zones in the developing human
691	cerebellum. Science. 366: 454-460. Doi: 10.1126/science.aax7526
692	Hata, A., J. Seoane, G. Lagna, E. Montalvo, A. Hemmati-Brivanlou et al., 2000 OAZ
693	uses distinct DNA- and protein-binding zinc fingers in separate BMP-Smad and
694	Olf signaling pathways. Cell. 100: 229-240. doi:10.1016/s0092-8674(00)81561-5
695	Hazen, V. M., M. G. Andrews, L. Umans, E. B. Crenshaw 3rd, A. Zwijsen et al., 2012
696	BMP receptor-activated Smads confer diverse functions during the development
697	of the dorsal spinal cord. Dev Biol. 367: 216-227.
698	doi:10.1016/j.ydbio.2012.05.014
699	Heydemann, A., L. C. Nguyen, and E. B. Crenshaw 3rd, 2001 Regulatory regions from
700	the Brn4 promoter direct LACZ expression to the developing forebrain and neural
701	tube. <i>Brain Res Dev Brain Res.</i> 128: 83-90. doi:10.1016/s0165-3806(01)00137-7
702	Hopp, K., C. M. Heyer, C. J. Hommerding, S. A. Henke, J. L. Sundsbak et al., 2011
703	B9D1 is revealed as a novel Meckel syndrome (MKS) gene by targeted exon-
704	enriched next-generation sequencing and deletion analysis. Hum Mol Genet. 20:
705	2524-2534. doi:10.1093/hmg/ddr151

- Horner, V. L., and T. Caspary, 2011 Disrupted dorsal neural tube BMP signaling in the
- cilia mutant Arl13b hnn stems from abnormal Shh signaling. *Dev Biol.* **355:** 43-
- 708 54. doi:10.1016/j.ydbio.2011.04.019
- Huang, S., J. Laoukili, M. T. Epping, J. Koster, M. Hölzel et al., 2009 ZNF423 is
- 710 critically required for retinoic acid-induced differentiation and is a marker of
- neuroblastoma outcome. *Cancer Cell.* **15**: 328-340.
- 712 doi:10.1016/j.ccr.2009.02.023
- Huangfu, D., A. Liu, A. S. Rakeman, N. S. Murcia, L. Niswander et al., 2003 Hedgehog
- signalling in the mouse requires intraflagellar transport proteins. *Nature.* **426**: 83-
- 715 87. doi:10.1038/nature02061
- Humbert, M. C., K. Weihbrecht, C. C. Searby, Y. Li, R. M. Pope et al., 2012 ARL13B,
- 717 PDE6D, and CEP164 form a functional network for INPP5E ciliary targeting. *Proc*
- 718 Natl Acad Sci U S A. **109:** 19691-19696. doi:10.1073/pnas.1210916109
- 719 Hynes, A. M., R. H. Giles, S. Srivastava, L. Eley, J. Whitehead et al., 2014 Murine
- Joubert syndrome reveals Hedgehog signaling defects as a potential therapeutic
- target for nephronophthisis. *Proc Natl Acad Sci U S A.* **111**: 9893-9898.
- 722 doi:10.1073/pnas.1322373111
- Ivanova, A. A., T. Caspary, N. T. Seyfried, D. M. Duong, A. B. West et al., 2017
- 724 Biochemical characterization of purified mammalian ARL13B protein indicates
- that it is an atypical GTPase and ARL3 guanine nucleotide exchange factor
- 726 (GEF). J Biol Chem. 292: 11091-11108. doi:10.1074/jbc.M117.784025
- 727 Kenney, A. M., and D. H. Rowitch, 2000 Sonic hedgehog promotes G(1) cyclin
- 728 expression and sustained cell cycle progression in mammalian neuronal

- 729 precursors. *Mol Cell Biol.* **20:** 9055-9067. doi:10.1128/mcb.20.23.9055-
- 730 9067.2000
- Lai, C. K., N. Gupta, X. Wen, L. Rangell, B. Chih et al., 2011 Functional
- characterization of putative cilia genes by high-content analysis. *Mol Biol Cell.*
- 733 **22:** 1104-1119. doi:10.1091/mbc.E10-07-0596
- Lan, Y., and R. Jiang, 2009 Sonic hedgehog signaling regulates reciprocal epithelial-
- 735 mesenchymal interactions controlling palatal outgrowth. *Development*. **136**:
- 736 1387-1396. doi:10.1242/dev.028167
- T37 Lancaster, M. A., D. J. Gopal, J. Kim, S. N. Saleem, J. L. Silhavy et al., 2011 Defective
- 738 Wnt-dependent cerebellar midline fusion in a mouse model of Joubert syndrome.
- 739 *Nat Med.* **17:** 726-731. doi:10.1038/nm.2380
- Li, Y., Q. Wei, Y. Zhang, K. Ling, and J. Hu, 2010 The small GTPases ARL-13 and
- 741 ARL-3 coordinate intraflagellar transport and ciliogenesis. *J Cell Biol.* **189:** 1039-
- 742 1051. doi:10.1083/jcb.200912001
- Li, Y., X. Tian, M. Ma, S. Jerman, S. Kong et al., 2016 Deletion of ADP ribosylation
- factor-like GTPase 13B leads to kidney cysts. *J Am Soc Nephrol.* **27**: 3628-3638.
- 745 doi:10.1681/ASN.2015091004
- Lipinski, R. J., C. Song, K. K. Sulik, J. L. Everson, J. J. Gipp et al., 2010 Cleft lip and
- palate results from Hedgehog signaling antagonism in the mouse: Phenotypic
- characterization and clinical implications. *Birth Defects Res A Clin Mol Teratol.*
- 749 **88:** 232-240. doi:10.1002/bdra.20656

- 750 Maria, B. L., K. B. Hoang, R. J. Tusa, A. A. Mancuso, L. M. Hamed et al., 1997 "Joubert
- 751 syndrome" revisited: key ocular motor signs with magnetic resonance imaging
- 752 correlation. J Child Neurol. **12:** 423-430. doi:10.1177/088307389701200703
- 753 Mariani, L. E., M. F. Bijlsma, A. A. Ivanova, S. K. Suciu, R. A. Kahn et al., 2016 Arl13b
- regulates Shh signaling from both inside and outside the cilium. *Mol Biol Cell.* 27:
- 755 3780-3790. doi:10.1091/mbc.E16-03-0189
- 756 Miertzschke, M., C. Koerner, M. Spoerner, and A. Wittinghofer, 2014 Structural insights
- into the small G-protein Arl13b and implications for Joubert syndrome. *Biochem*
- 758 *J.* **457:** 301-311. doi:10.1042/BJ20131097
- 759 Munoz-Estrada, J., and R. J. Ferland, 2019 Ahi1 promotes Arl13b ciliary recruitment,
- regulates Arl13b stability and is required for normal cell migration. *J Cell Sci.*
- 761 **132:** jcs230680. doi:10.1242/jcs.230680
- Nolan-Stevaux, O., J. Lau, M. L. Truitt, G. C. Chu, M. Hebrok et al., 2009 Gli1 is
- regulated through Smoothened-independent mechanisms in neoplastic
- 764 pancreatic ducts and mediates PDAC cell survival and transformation. *Genes*
- 765 Dev. 23: 24-36. doi:10.1101/gad.1753809
- 766 Nuovo, S., I. Bacigalupo, M. Ginevrino, R. Battini, E. Bertini et al., 2020 Age and sex
- prevalence estimate of Joubert syndrome in Italy. *Neurology*. **94:** e797-e801.
- 768 doi:10/1212/WNL.00000000008996
- 769 Onimaru, H., Y. Kumagawa, and I. Homma, 2006 Respiration-related rhythmic activity
- in the rostral medulla of newborn rats. *J Neurophysiol.* **96:** 55-61.
- 771 doi:10.1152/jn.01175.2005

- 772 Otto, E. A., K. Tory, M. Attanasio, W. Zhou, M. Chaki et al, 2009 Hypomorphic
- 773 mutations in meckelin (MKS3/TMEM67) cause nephronophthisis with liver
- fibrosis (NPHP11). *J Med Genet.* **46:** 663-670. doi:10.1136/jmg.2009.066613
- Parisi, M. A, 2019 The molecular genetics of Joubert syndrome and related ciliopathies:
- The challenges of genetic and phenotypic heterogeneity. *Transl Sci Rare Dis.* **4**:
- 777 25-49. doi:10.3233/TRD-190041
- Parisi, M. A., D. Doherty, P. F. Chance, and I. A. Glass, 2007 Joubert syndrome (and
 related disorders) (OMIM 213300). *Eur J Hum Genet.* 15: 511-521.
- 780 doi:10.1038/sj.ejhg.5201648
- 781 Pasqualato, S., L. Renault, and J. Cherfils, 2002 Arf, Arl, Arp and Sar proteins: A family
- of GTP-binding proteins with a structural device for 'front-back' communication.
- 783 *EMBO Rep.* **3:** 1035-1041. doi:10.1093/embo-reports/kvf221
- 784 Poretti, A., E. Boltshauser, T. Loenneker, E. M. Valente, F. Brancati et al., 2007
- 785 Diffusion tensor imaging in Joubert syndrome. *AJNR Am J Neuroradiol.* 28:
- 786 1929-1933. doi:10.3174/ajnr.A0703
- 787 Quisling, R. G., A. J. Barkovich, and B. L. Maria, 1999 Magnetic resonance imaging
- 788 features and classification of central nervous system malformations in Joubert
- 789 syndrome. *J Child Neurol.* **14:** 628-635. doi:10.1177/088307389901401002
- 790 Rafiullah, R., A. B. Long, A. A. Ivanova, H. Ali, S. Berkel et al., 2017 A novel
- homozygous ARL13B variant in patients with Joubert syndrome impairs its
- guanine nucleotide-exchange factor activity. *Eur J Hum Genet.* **25**: 1324-1334.
- 793 doi:10.1038/s41431-017-0031-0

794	Ramsbottom, S. A., P. E. Thelwall, K. M. Wood, G. J. Clowry, L. A. Devlin et al., 2020
795	Mouse genetics reveals Barttin as a genetic modifier of Joubert syndrome. Proc
796	Natl Acad Sci U S A. 117: 1113-1118. doi:10.1073/pnas.1912602117
797	Reiter, J. F., and W. C. Skarnes, 2006 Tectonic, a novel regulator of the Hedgehog
798	pathway required for both activation and inhibition. Genes Dev. 20: 22-27.
799	doi:10.1101/gad.1363606
800	Roberson, E. C., W. E. Dowdle, A. Ozanturk, F. R. Garcia-Gonzalo, C. Li et al., 2015
801	TMEM231, mutated in orofaciodigital and Meckel syndromes, organizes the
802	ciliary transition zone. J Cell Biol. 209: 129-142. doi:10.1083/jcb.201411087
803	Sang, L., J. J. Miller, K. C. Corbit, R. H. Giles, M. J. Brauer et al., 2011 Mapping the
804	NPHP-JBTS-MKS protein network reveals ciliopathy disease genes and
805	pathways. Cell. 145: 513-528. doi:10.1016/j.cell.2011.04.019
806	Schindelin, J., I. Arganda-Carreras, E. Frise, V. Kaynig, M. Longair et al., 2012 Fiji: an
807	open-source platform for biological-image analysis. Nat Methods. 9: 676-682.
808	doi:10.1038/nmeth.2019
809	Schrick, J. J., P. Vogel, A. Abuin, B. Hampton, and D. S. Rice, 2006 ADP-ribosylation
810	factor-like 3 is involved in kidney and photoreceptor development. Am J Pathol.
811	168: 1288-1298. doi:10.2353/ajpath.2006.050941
812	Schwarz, N., A. Lane, K. Jovanovic, D. A. Parfitt, M. Aguila et al., 2017 Arl3 and RP2
813	regulate the trafficking of ciliary tip kinesins. Hum Mol Genet. 26: 2480-2492.
814	doi:10.1093/hmg/ddx143

- Shaheen, R., K. Szymanska, B. Basu, N. Patel, N. Ewida et al., 2016 Characterizing
 the morbid genome of ciliopathies. *Genome Biol.* 17: 242. doi:10.1186/s13059016-1099-5
- 818 Srour, M., F. F. Hamdan, J. A. Schwartzentruber, L. Patry, L. H. Ospina et al., 2012
- 819 Mutations in TMEM231 cause Joubert syndrome in French Canadians. *J Med*
- 820 *Genet.* **49:** 636-641. doi:10.1136/jmedgenet-2012-101132
- 821 Su, C-Y., S. N. Bay, L. E. Mariani, M. J. Hillman, and T. Caspary, 2012 Temporal
- deletion of Arl13b reveals that a mispatterned neural tube corrects cell fate over

time. *Development.* **139:** 4062-4071. doi:10.1242/dev.082321

- Thomas, S., V. Cantagrel, L. Mariani, V. Serre, J-E. Lee et al., 2015 Identification of a
- 825 novel ARL13B variant in a Joubert syndrome-affected patient with retinal
- impairment and obesity. *Eur J Hum Genet.* **23:** 621-627.
- 827 doi:10.1038/ejhg.2014.156
- Thomas, S., M. Legendre, S. Saunier, B. Bessières, C. Alby et al., 2012 TCTN3
- 829 mutations cause Mohr-Majewski syndrome. *Am J Hum Genet.* **91:** 372-378.
- 830 doi:10.1016/j.ajhg.2012.06.017
- Valente, E. M., F. Brancati, and B. Dallapiccola, 2008 Genotypes and phenotypes of

Joubert syndrome and related disorders. *Eur J Med Genet.* **51:** 1-23.

- 833 doi:10.1016/j.ejmg.2007.11.003
- Valente, E. M., C. V. Logan, S. Mougou-Zerelli, J. H. Lee, J. L. Silhavy et al., 2010
- 835 Mutations in TMEM216 perturb ciliogenesis and cause Joubert, Meckel and
- related syndromes. *Nat Genet.* **42:** 619-625. doi:10.1038/ng.594

837	Vierkotten, J., R. Dildrop, T. Peters, B. Wang, and U. Rüther, 2007 Ftm is a novel basal
838	body protein of cilia involved in Shh signaling. Development. 134: 2569-2577.
839	doi:10.1242/dev.003715
840	Weatherbee, S. D., L. A. Niswander, and K. V. Anderson, 2009 A mouse model for
841	Meckel syndrome reveals Mks1 is required for ciliogenesis and Hedgehog
842	signaling. <i>Hum Mol Genet</i> . 18: 4565-4575. doi:10.1093/hmg/ddp422
843	Wechsler-Reya, R. J., and M. P. Scott, 1999 Control of neuronal precursor proliferation
844	in the cerebellum by Sonic Hedgehog. Neuron. 22: 103-114. doi:10.1016/s0896-
845	6273(00)80682-0
846	Wu, C., M. Yang, J. Li, C. Wang, T. Cao et al., 2014 Talpid3-binding centrosomal
847	protein Cep120 is required for centriole duplication and proliferation of cerebellar
848	granule neuron progenitors. PLoS One. 9: e107943.
849	doi:10.1371/journal.pone.0107943
850	Yachnis, A. T., and L. B. Rorke, 1999 Neuropathology of Joubert syndrome. J Child
851	Neurol. 14: 655-659. doi:10.1177/088307389901401006
852	Zhang, X. M., M. Ramalho-Santos, and A. P. McMahon, 2001 Smoothened mutants
853	reveal redundant roles for Shh and Ihh signaling including regulation of L/R
854	symmetry by the mouse node. Cell. 106: 781-792.
855	Zhu, J., HT. Wang, YR. Chen, LY. Yan, YY. Han et al., 2020 The Joubert
856	syndrome gene arl13b is critical for early cerebellar development in zebrafish.
857	Neurosci Bull. 36: 1023-1034. doi:10.1007/s12264-020-00554-y
858	

859 Figure legends

860 Figure 1: SCPs lacking *Arl13b* or *Smo* fail to project to the dorsal thalamus. (A-C)

861 Schematics of injections and fluorescent tracer diffusion shown horizontally (A) or 862 sagittally (B-C). (A) Red dashed arrow depicts dye path in a successful injection from 863 injection site (red X) caudal through the brain and across the midline and into the 864 contralateral cerebellar DCN (red arrowhead). Grey background boxes indicate area of 865 subsequent images: the injection site (INJ) and cerebellum (DCN). (D-I) Representative 866 images of dorsal (D, F, H) or ventral (E, G, I) thalamus injection site (top panel) and 867 cerebellum (middle panel) with the DCN in hatched white circle and magnified (bottom 868 panel) with recoloring to black and white to aid visualization. The retrograde fluorescent 869 tracer is pink-red and sections are stained with DAPI (blue). Numbers indicate the 870 number of positively stained DCN clusters (DCN traced) out of the total number of 871 injected animals. Note that no tracing was observed on ipsilateral side to injection. (D. E) Fluorescent tracer injection in Smo^{fl/+}; Arl13b^{fl/+}; Nex-Cre control animals resulted in 872 873 contralateral DCN staining in (D) 6/8 dorsal thalamus injections and (E) 8/11 ventral 874 thalamus injections. (F, G) Fluorescent tracer injection in Smo^{Nex-Cre} animals resulted in 875 contralateral DCN staining in (F) 0/6 dorsal thalamus injections and (G) 4/4 ventral thalamus injections. (H, I) Fluorescent tracer injection in Arl13b^{Nex-Cre} animals resulted in 876 877 contralateral DCN staining in (H) 1/7 dorsal thalamus injections and (I) 4/4 ventral 878 thalamus injections. Two-tailed Fisher's exact test was performed; only the dorsal 879 injection results were significantly different from the controls (F: p<0.01; H: p<0.05) 880

Figure 2: SCPs expressing cilia-excluded ARL13B^{V358A} project normally to both
 the dorsal and ventral thalamus. (A-D) Representative images of dorsal (A, C) or

41

883 ventral (B, D) thalamus injection site (top panel) and cerebellum (middle panel) with the 884 DCN in hatched white circle and magnified (bottom panel) with recoloring to black and 885 white to aid visualization. Numbers indicate the number of positively stained DCN 886 clusters out of the total number of injected animals. Note that no tracing was observed on the injection's ipsilateral side. (A, B) Fluorescent tracer injection in Arl13b^{V358A/+} 887 888 control animals resulted in contralateral DCN staining in (A) 3/3 dorsal thalamus 889 injections and (B) 4/4 ventral thalamus injections. (C-D) Fluorescent tracer injection in Arl13b^{V358A/V358A} animals resulted in contralateral DCN staining in (C) 4/4 dorsal 890 891 thalamus injections (Fisher's exact test, two-tailed, ns, p>0.9) and (D) 3/3 ventral 892 thalamus injections (ns, p>0.9).

893

Figure 3: SCPs expressing JS allele *Arl13b*^{*R79Q*} project normally to both the dorsal 894 895 and ventral thalamus. (A) Schematic showing the protein domain structure of Arl13b. 896 The R79Q mutation occurs in a highly conserved subregion of the GTPase domain, 897 Switch 2 (red). (B) Alignment of protein sequence surrounding amino acid 79 of mouse 898 Arl13b (red highlight) showing that arginine is conserved across multiple species. 899 Sequences used in protein alignment: Homo sapiens NP 878899.1, Mus musculus NP 080853.3, Danio rerio NP 775379.1, Chlamydomonas reinhardtii XP 001691430.1. 900 901 (C-F) Representative images of dorsal (C, E) or ventral (D, F) thalamus injection site 902 (top panel) and cerebellum (middle panel) with the DCN in hatched white circle and 903 magnified (bottom panel) with recoloring to black and white to aid visualization. 904 Numbers indicate the number of positively stained DCN clusters out of the total number 905 of injected animals. Note that no tracing was observed on the injection's ipsilateral side.

906	(C, D) Fluorescent tracer injection in Arl13b ^{R79Q/+} control animals resulted in
907	contralateral DCN staining in (C) 4/4 dorsal thalamus injections and (D) 3/3 ventral
908	thalamus injections. (E-F) Fluorescent tracer injection in Arl13b ^{R79Q/R79Q} animals
909	resulted in contralateral DCN staining in (E) 3/3 dorsal thalamus injections (Fisher's
910	exact test, two-tailed, ns, p>0.9) and (F) 3/4 ventral thalamus injections (ns, p>0.9).
911	
912	Figure 4: Mouse embryos expressing JS allele <i>Arl13b^{R79Q}</i> display normal cell
913	patterning in the neural tube. Shh, Olig2, Pax6 and Arl13b staining of E10.5 Arl13b ^{+/+}
914	(n=3), <i>Arl13b</i> ^{R79Q/R79Q} (n=3), <i>Arl13b</i> ^{R79Q/A} (n=3), and <i>Arl13b</i> ^{A/A} (n=3) mouse neural tubes.
915	Scale bar = 100 micrometers in A-L or 10 micrometers in M-P. (A-D) Shh is visible in the
916	notochord and floorplate of (A) $Arl13b^{+/+}$, (B) $Arl13b^{R79Q/R79Q}$ and (C) $Arl13b^{R79Q/\Delta}$ neural
917	tubes but absent from the floorplate of (D) $Arl13b^{\Delta/\Delta}$ embryos. (E-H) Olig2 stains the
918	motor neuron precursor domain in (E) $Arl13b^{+/+}$, (F) $Arl13b^{R79Q/R79Q}$ and (G) $Arl13b^{R79Q/\Delta}$
919	embryos and stains an expanded domain in (H) $Arl13b^{\Delta/\Delta}$ embryos. (I-L) Pax6
920	expression is visible in the dorsal neural tube in (I) $Arl13b^{+/+}$, (J) $Arl13b^{R79Q/R79Q}$ and (K)
921	<i>Arl13b</i> ^{R79Q/Δ} neural tubes but shifted dorsally in (L) <i>Arl13b</i> ^{Δ/Δ} neural tubes. (M-P) Arl13b
922	is localized to cilia visible in the ventral lumen of (M) Arl13b ^{+/+} , (N) Arl13b ^{R79Q/R79Q} and
923	(O) $Arl13b^{R79Q/\Delta}$ neural tubes but absent from (P) $Arl13b^{\Delta/\Delta}$ embryos.
924	

Figure 5: *Arl13b*^{R79Q} mutation does not affect cerebellar width. (A) Representative
surface-facing images of cerebella from control and *Arl13b*^{R79Q/R79Q} mutant mice.
Scalebar = 1mm, black line indicates where cerebellar width was measured, red line
indicates where vermis width was measured, gray line indicates where cerebellar

43

hemisphere height was measured, blue line indicates where vermis height was
measured. (B) Ratios of *Arl13b*^{R79Q/R79Q} mutant to control measurements of sex- and
age-matched pairs of mice showed no significant difference. Cerebellar and vermis
measurements were determined from surface views (symbol colors match the lines in
A), body and dissected brain weights were determined using a standard lab scale. Each
symbol represents a pair of sex- and age-matched animals: females are represented as
circles and males are represented as triangles.

936

937 Figure 6: Pan-neuronal deletion of *Arl13b* results in a small cerebellum. (A)

938 Representative images of cerebella from control and *Arl13b^{Brn4-Cre}* mutant mice.

939 Scalebar = 1mm. (B) The ratio of *Arl13b*^{Brn4-Cre} mutant to control cerebellar width was

940 reduced in both females and males (one-sample t-test: p<0.1, single asterisk). The ratio

941 of *Arl13b^{Brn4-Cre}* mutant to control vermis width was reduced in female and male age

942 matched pairs (one-sample t-test: p<0.0001, four asterisks). While *Arl13b^{Bm4-Cre}* mutants

had moderately lower body weights than controls (one-sample t-test: p<0.1, single

944 asterisk), their brains were slightly heavier, likely due to hydrocephaly. Each symbol

945 represents a pair of sex- and age-matched animals: females are represented as circles

946 and males are represented as triangles.

947

948 Figure 7: Mice expressing cilia-excluded *Arl13b*^{V358A} have cerebella of normal

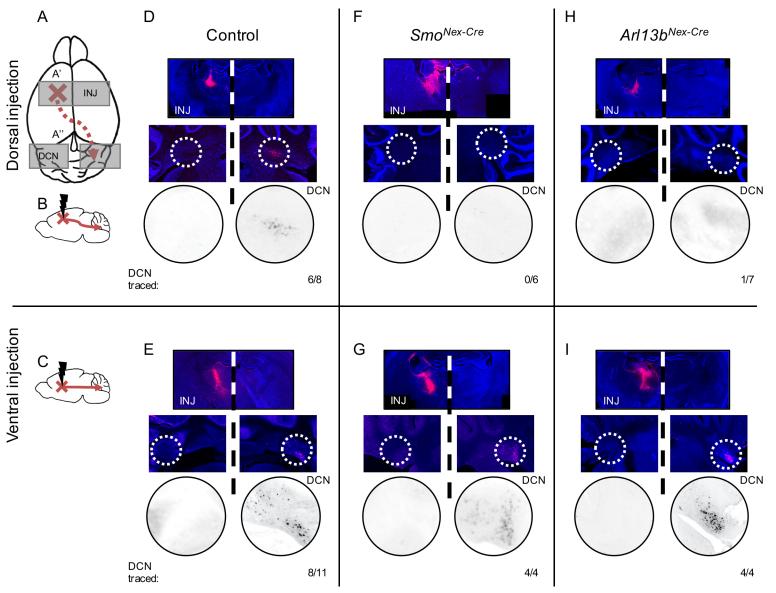
949 width. (A) Representative images of cerebella from control and *Arl13b*^{V358A/V358A} mutant

950 mice. Scalebar = 1mm. (B) Ratios of $Arl13b^{V358A/V358A}$ mutant to control measurements

951 of sex- and age-matched pairs of mice showed no significant differences (one-sample t-

- 952 test). Each dot represents a pair of sex- and age-matched animals: females are
- 953 represented as circles and males are represented as triangles.

954



bioRxiv preprint doi: https://doi.org/10.1101/2021.01.29.428892; this version posted April 28, 2021. The copyright holder for this preprint (which was not certified by peer review) is the author/funder, who has granted bioRxiv a license to display the preprint in perpetuity. It is made A Ar/13b^{V358,4/V358,4}

